ELSEVIER

Contents lists available at ScienceDirect

Superconductivity

journal homepage: www.elsevier.com/locate/supcon



Full Length Article

Electrical, magnetic and thermal circuit modelling of a superconducting halfwave transformer rectifier flux pump using Simulink



A.C. Francis ^{a,*}, S. Venuturumilli ^{a,c}, D.A. Moseley ^a, S. Claridge ^a, B. Leuw ^{a,c}, R.A. Badcock ^a, C.W. Bumby ^{a,b}

- ^aRobinson Research Institute, Victoria University of Wellington, 69 Gracefield Road, Lower Hutt 5010, New Zealand
- b MacDiarmid Institute, Victoria University of Wellington, Wellington 6140, New Zealand
- ^c Open Star Technologies Limited, Ngauranga 6035, Wellington, New Zealand

ARTICLE INFO

Keywords: Simulink Simscape Thermal Jc(B) switch Flux pump High-temperature superconductivity

ABSTRACT

Superconducting flux pumps (FP) are capable of supplying superconducting circuits with high currents by additively supplying current over a number of cycles without introducing large amounts of heat into the cryogenic environment. Superconducting FPs can be broadly classified into two types: dynamo and transformer rectifier. Modelling the behaviour of these systems is an emerging field. In this work a model of a half wave magnetically switched transformer rectifier FP created in MATLAB/Simulink/Simscape is presented. Unlike existing models, the characteristics of all circuit elements are fully integrated allowing all superconducting elements to be accurately incorporated. The presented method uses pre-calculated look-up tables, populated with experimentally derived material qualities to simulate these superconducting elements. The thermal evolution of the switches, calculated simultaneously to the magnetic field switching interaction has also been included. This model is compared to the performance of a real world FP during the pumping of a load coil and is found to be accurate. Furthermore, the presented model illustrates how small amounts of heating at a magnetic switch can profoundly affect a FPs performance over many cycles.

1. Introduction

High field magnets are used in many applications including fusion energy, magnetic levitation, magnetic resonance imaging, nuclear magnetic resonance, high energy and nuclear physics [1–7]. High temperature superconductors (HTS) are increasingly being considered for these applications due to their operating temperatures and critical fields [8]. To maximise the potential of HTS magnets large currents are required [1]. Conventional high current power supplies, while widely available, are large and expensive. The current leads from these power supplies, usually made of copper, introduce significant amounts of heat into the cryogenic environment which must be accounted for. This is a large issue as HTS magnets must be kept at cryogenic temperatures to remain superconducting [9]. The large heat load from ohmic leads increases the cost and complexity of the required cooling systems [10].

Superconducting flux pumps (FPs) operate in the same cryogenic environment as a HTS magnet introducing far less of a heat load [11]. HTS circuits and components require joints between the HTS tapes they are constructed from. Although purely superconducting joints are possible [12], most HTS systems are usually made with soldered joints with a small ohmic resistance causing a loss of current. To maintain a stable

field value in a HTS magnet this loss must be countered with continuous charging [4,13–15]. Superconducting flux pumps are an ideal solution for solving the issue of resistive joint loss [16].

The concept of superconducting flux pumps has existed since the 1950s [17,18] and has seen a resurgence with the introduction of HTS systems [19]. The higher operating temperature and large enthalpy of HTS allows for a variety of operational pumping principles [20]. These fall into two main classes: (i) Dynamo and travelling wave flux pumps [19,21–24] and (ii) transformer rectifier flux pumps (TRFPs) [25–27].

These two classes work in distinct ways. Dynamo and travelling wave flux pumps induce a net non-zero voltage with a moving magnetic field [28], while TRFPs use a transformer to generate a large DC current in a load via rectification of an alternating current. TRFPs can be either full-wave where the full alternating current cycle is used for rectification or half-wave where only half of the cycle is utilised. Currently, five switching techniques have been published for TRFPs being; the utilisation of non-superconducting MOSFET arrays [25], thermal switching [29], self-switching [30,27], applied alternating magnetic field switching (dynamic resistance) [31–33] and applied static magnetic field switching ($J_c(B)$) [34].

E-mail address: adam.francis@vuw.ac.nz (A.C. Francis).

^{*} Corresponding author.

Creating precisely controlled HTS TRFPs is difficult without an accurate modelling tool to effectively define the experimental parameters required to meet the desired specifications. This work introduces one such simulation constructed in MATLAB/Simulink [35], with additional custom Simscape blocks. This model simulates a half-wave $J_c(B)$ switched TRFP over many cycles. The effective capture of the highly non-linear HTS behaviour is the main challenge for such a model. Previous simulations have utilised SPICE [36,37] or analytical approximations of the HTS behaviour [38,39] to qualitatively match experiment findings. The presented model attempts to increase the accuracy of simulation by using experimentally derived superconducting properties to create look-up tables of resistivity for all superconducting components. Although look-up tables are well established in finite element modelling, this is the first time that they have been utilised in this context.

A similar simulation for a half wave TRFP has been discussed recently [40], however it does not take into account $J_c(B)$ switches, thermal effects at the switches or use a magnetic circuit to represent the transformer. The simulation presented in the following pages includes all of these aspects in an attempt to create a more realistic model.

2. Half-wave $J_c(B)$ rectification

A half-wave TRFP takes an alternating primary current ($I_{\rm pri}$) waveform and converts it into a direct load current ($I_{\rm L}$) via an alternating secondary current ($I_{\rm sec}$). This is achieved by separating the waveform into two distinct phases (rectification and maintenance) and activating two resistive switches placed in parallel ($R_{\rm p}$) and in series ($R_{\rm s}$) with the load. During the rectification phase the load coil is charged via the potential generated by the parallel switch forcing the transformer into a magnetised state. During the maintenance phase the transformer is forced back towards a demagnetised state via the voltage generated by the series switch allowing repeated charging cycles to be utilised. Complete demagnetisation is only possible if the core B(H) profile is considered to be anhysteretic [41], as a hysteretic core will never return to a zero state during operation without some very clever system manipulation and control [42]. Over successive cycles a half-wave TRFP will pump $I_{\rm L}$ up in a step like manner [34].

The use of a transformer in a step down configuration (more primary turns $(N_{\rm pri})$ than secondary turns $(N_{\rm sec})$) allows for a large $I_{\rm sec}$ and sub-sequentially a large $I_{\rm L}$ to be generated whilst using a small $I_{\rm pri}$. An electrical circuit diagram of a half-wave TRFP is shown in Fig. 1.

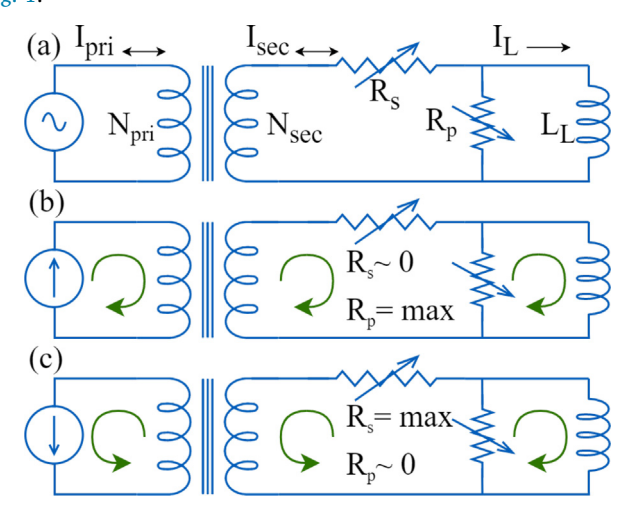


Fig. 1. (a) Shows the TRFP electrical circuit detailing various components. (b) and (c) are half cycle representations of the same system where (b) illustrates the current direction during the rectification phase and (c) the maintenance phase.

Throughout this work, we will be comparing the performance of the simulation to experimental data derived from a $J_c(B)$ switched TRFP. A more detailed overview of this experimental system is provided in Leuw et al. [34]. While the experimental set-up remains identical to this work we have generated new datasets. In the work by Leuw et al. [34], the focus was on illustrating the ultimate performance of the TRFP which involved driving the system to its limits. This process generated significant amounts of heating making accurate simulation difficult. To eradicate this issue, we have taken new data utilising smaller primary currents which, as will be illustrated later, lead to a more stable performance which can be simulated.

3. Model description

The half-wave $J_c(B)$ TRFP model is built within the MATLAB/Simulink platform and includes various custom Simscape 'blocks' in combination with the Simscape electrical, magnetic and thermal libraries. The model is constructed around 5 fundamental elements: input waveform creation and implementation, the transformer magnetic circuit block, the electrical secondary circuit, superconducting component blocks and thermal circuit blocks which interact with the superconducting components. The visual Simulink code for all parts of the model are displayed in the appendix (see Figs. A.13,A.14,A.15,A.16.

3.1. Input waveforms

The input waveform blocks are designed to allow the application of any desired waveform combination. In this work, the experimental waveforms of transformer primary current and the electromagnetic switch fields as derived from direct measurement were used to drive the simulation. This ensures complete consistency between the simulation and experiment. The precise structure of the applied waveforms are displayed in Fig. 2. In this case, for all input waveforms the positive primary half-wave is aligned with the series electromagnet 'on' state, and the negative half-wave with the parallel electromagnet 'on'. This formulation will produce a negative load current.

3.2. Transformer primary and magnetic circuit

The transformer model is broken up into three parts; the primary winding, the transformer core and the secondary winding and is represented with a circuit diagram in Fig. 3.

The Simulink code allows any configuration of transformer winding configuration and core behaviour. In the experimental system, the core is made of laminated electrical steel with a reluctance

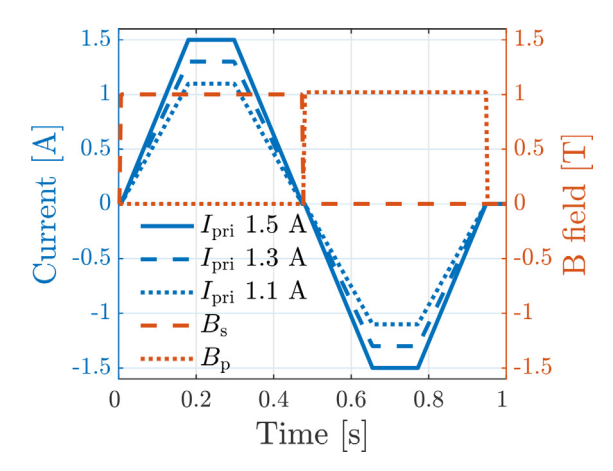


Fig. 2. Experimentally generated input waveforms for the transformer primary (blue) and the electromagnets (red) for two different time distributions of maximised (a) and smaller(b) switch ramp rates.

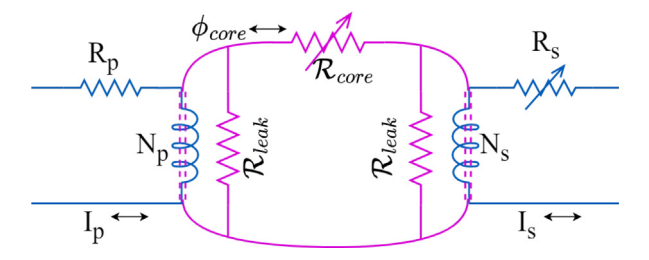


Fig. 3. Circuit model for the transformer, linking both the electrical (blue) and magnetic (pink) circuits with constant copper primary resistance and dynamic secondary HTS resistance.

 (\mathcal{R}_{core}) determined by the transformer core material, length and cross-sectional area. In the model an experimentally measured anhysteretic B(H) curve with a B field saturation of ~ 1.8 T and a H field saturation turning point of ~ 200 A/m is used. This is input into the 'Non-linear Reluctance' block from the Simscape magnetic element library.

In the experimental work discussed below, the primary winding is driven in constant current mode where the power supply voltage ramps automatically to achieve the selected current. In the model this is implemented as a constant current source with a primary winding ohmic resistance ($R_{\rm pri}$) of zero. This is zero due to the input primary current waveform being taken from an experimental measurement of the primary current directly using a known resistor as shown in Fig. 2 in blue.

The experimental primary winding (N_{pri}) is made of 720 turns of enamelled copper while the secondary winding (N_{sec}) consists of 12 turns of 12 mm SuNAM copper coated superconducting tape. The secondary winding has a variable resistance (R_s) caused by the non-linear superconducting resistance. The HTS R_s is handled through the use of a custom Simscape block the workings of which will be explained in the following section. As in many transformer-rectifier flux pumps, the experimental secondary current does not match the basic $N_{\rm pri}N_{\rm sec}$ ratio [34,43]. Furthermore, the model, as it stands, is also incapable of capturing the observed behaviour. Instead, we arbitrarily set the modelled secondary winding to 17 turns to match the experimental secondary current. Further additions to the model are planned to capture this variation. However, once this static mismatch is accounted for, the model is highly effective at simulating the dynamic processes within the transformer. For instance, the remnant magnetization within in the transformer core which leads to the creation of a DC offset is accurately captured.

The leakage flux (\mathcal{R}_{leak}) is included for both the primary and secondary windings calculated from the geometry of the system and the medium that the stray fields pass through, in this case liquid nitrogen (LN2). The assumption has been made that eddy current loss will have a small impact due to the core material and construction type, being laminated electrical steel, and has therefore been omitted.

3.3. HTS Elements

The performance of the model is dictated primarily by the HTS tape used and how an applied magnetic field and applied current interacts with it. When the applied magnetic field penetrates the superconducting layer of a HTS tape some of the current is pushed into the ohmic layers. These ohmic layers are required for passivation and electrical and mechanical stabilisation [44] as shown in Fig. 4. Surface passivation of HTS films prevents unwanted reactions with carbon dioxide and water in the atmosphere which can damage the superconducting material [45].

As most of these layers are electrically conductive this layered structure provides additional electrical paths parallel to the superconducting layer. These parallel paths have their own resistance, collec-

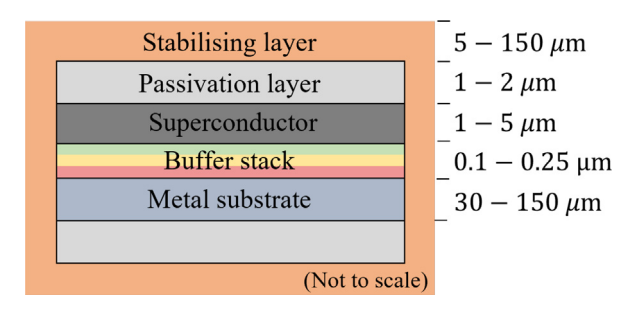


Fig. 4. Generic coated superconductor architecture comprised of a metal substrate for mechanical support, a stack of intermediate buffer layers to provide planarisation, passivation and texturing, the superconductor, a further passivation layer and an electrical stabilisation layer. Inspired by MacManus-Driscoll and Wimbush [44].

tively called the ohmic resistance path $(R_{\rm oh})$. To physically model the behaviour of the $J_c(B)$ rectifier $R_{\rm oh}$ must be included by combining it with the superconductor resistance $(R_{\rm sc})$ to calculate a total resistance $(R_{\rm T})$. $R_{\rm oh}$ and $R_{\rm sc}$ cannot be measured separately through experiment when operating the TRFP, presenting a problem to $J_c(B)$ switched simulations. What can be measured experimentally is the voltage $(V_{\rm E})$ across a switch and the total applied current $(I_{\rm T})$, which is the sum of the current in the superconducting layer $I_{\rm sc}$ and the ohmic paths $I_{\rm oh}$. These variables are illustrated in Fig. 5(a) along with a simple circuit diagram for a section of HTS tape.

Normally when considering a HTS system $I_{\rm oh}$ and $R_{\rm oh}$ are not considered as all of the current is assumed to travel through the superconductor. While this is a fine assumption to make for HTS systems that operate far from their critical current (I_c) , it is not applicable for a $J_c(B)$ switched system or one that operates at temperatures close to their critical temperature. In these systems the I_c of the system can change dramatically forcing current into the parallel ohmic paths. From a modelling perspective this manifests as a circularity problem where the parallel resistances cannot be determined without the parallel currents, as illustrated in Fig. 5(b). This circularity originates as $R_{\rm sc}$ is dependent on the fraction of $I_{\rm T}$ entering the superconducting path $(I_{\rm co})$:

$$R_{\rm sc}(I_{\rm sc}) = \frac{E_0 \ell_{\rm tape}}{I_{\rm c}(B)} \left(\frac{I_{\rm sc}}{I_{\rm c}(B)}\right)^{n(B)-1},\tag{1}$$

where E_0 is the electric field criterion set to $1~\mu \rm{Vcm}^{-1}$, n is the so-called n-value which defines the superconductor behaviour in its non-linear resistivity state, B is the magnetic field experienced by the HTS element and $\ell_{\rm tape}$ is the length of the superconducting element considered.

In contrast, R_{oh} simply follows the standard ohmic law considerations:

$$R_{\rm oh} = \frac{\rho_{\rm oh} \ell_{\rm tape}}{w_{\rm tane} \tau_{\rm oh}},\tag{2}$$

where $\rho_{\rm oh}$ is the resistivity of the stabilizer material, $w_{\rm tape}$ is the width of the ohmic layers and $\tau_{\rm oh}$ is the thickness of the ohmic layers. The parallel stabiliser path leads to the total resistance having the form;

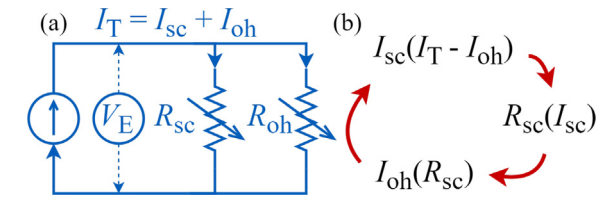


Fig. 5. (a) Parallel current paths through the ohmic and super conductor layers. (b) Circularity problem that arises when attempting to find either $R_{\rm oh}$ or $R_{\rm sc}$ from experimentally derived $I_{\rm T}$ and $V_{\rm E}$ values.

$$R_{\rm T}(I_{\rm sc}) = \frac{R_{\rm sc}(I_{\rm sc})R_{\rm oh}}{R_{\rm sc}(I_{\rm sc}) + R_{\rm oh}}.$$
 (3)

Using equations Eqs. (1)–(3), in conjunction with the fact that the voltage across both paths $(V_{\rm E})$ must be equivalent, $I_{\rm Sc}$ can be calculated numerically from;

$$\frac{\ell_{\text{tape}} E_0}{R_{\text{oh}} I_{\text{c}}^n(B)} I_{\text{sc}}^{n(B)} + I_{\text{sc}} = I_{\text{T}}. \tag{4}$$

From a modelling perspective $I_{\rm sc}$ could be calculated for each superconducting element at each time step. However, this is computationally intensive and would significantly increase simulation time.

Instead, a more practical approach is to generate a lookup table during the initialisation of the model. This can be achieved as $R_{\rm sc}$ is uniquely defined for all $I_{\rm sc}$ for the configuration outlined in Fig. 5 (a). Using Eq. 1, $R_{\rm sc}$ can be calculated for a pre-determined range of $I_{\rm sc}$ values (0.01 to 1.2 times $I_{\rm c}$ has been found to be sufficient). By utilising the voltage equivalency, each $R_{\rm sc}$ value can be related to a specific $I_{\rm ob}$ value;

$$I_{\rm oh} = \frac{R_{\rm sc}I_{\rm sc}}{R_{\rm oh}},\tag{5}$$

from which a corresponding I_T can be ascertained;

$$I_{\rm T} = I_{\rm oh} + I_{\rm sc}. \tag{6}$$

Finally, $R_{\rm T}$ can be calculated from Eqs. 6,. By iteratively applying this process for each $I_{\rm sc}$ value, a lookup table for a input $I_{\rm T}$ value can be uniquely correlated to a $R_{\rm T}$ value which defines the superconducting element performance. If $V_{\rm E}$ is required this can be simply calculated by;

$$V_{\rm E} = I_{\rm T} R_{\rm T}.\tag{7}$$

The lookup table is generated during the initialisation of the Simulink model. Constructing the lookup table before the simulation is run drastically reduces the computational requirements of the model when compared to a version that calculates the resistance at each time step. The presented results in the following section were made with time steps of 1 ms.

For the load coil (constructed with brass stabilised 4.4 mm AMSC YBCO tape [46,47]) and transformer secondary winding (constructed with copper stabilised 12 mm SuNAM YBCO tape) using a lookup table of only one temperature is deemed sufficient. This is because in experiment both elements operate far below $I_{\rm c}$ and the variations in $I_{\rm c}({\rm T,B})$ or $n({\rm T,B})$ are not as significant. However, within the switching elements this is not the case as the magnetic field and temperature dependencies play fundamental roles in determining the flux pump performance and must be accounted for.

A significant advantage of the lookup table approach is that it allows the introduction of these variables in a simple and noncomputationally intensive manner. To introduce the influence of magnetic field it is simply a case of repeating the process outlined above for a range of $I_c(B)$ and n(B) values in conjunction with the I_{Sc} iteration. This will generate a 2D lookup table from which R_T can be found for the input I_T and B at each time step. In the outlined simulation the range of magnetic field intensities is 0 to 1.5 T to cover the range used in experiment of 0 to 1 T. This lookup table can be further increased into a 3D data set inclusive of temperature by stacking multiple 2D magnetic field dependency arrays at different temperatures together to make a 3D array containing both temperature and magnetic field dependence.

To fill out such a table with realistic values the Robinson Research Institute SuperCurrent database (https://www.wgtn.ac.nz/robinson/hts-wire-database) [48] has been used. This data base contains experimentally derived $I_c(T,B,\theta)$ and $n(T,B,\theta)$ data for many different HTS tapes, the switch tape that is used in this work is 6 mm SuNAM HCN04200. As the experimental system has a geometrically static magnetic field perpendicular to the planar tape surface only the

 $I_{\rm c}(T,B,0)$ and n(T,B,0) data is used. A plot of this $I_{\rm c}(T,B,0)$ data is shown in Fig. 6.

As the system is modelled with a stable magnetic field angle the $I_{\rm sc}$ values are iterated through as above for each set of $I_{\rm c}(T,B)$ and n(T,B) to produce the lookup table which can provide the $R_{\rm T}$ for any applied magnetic field, temperature or input current. When considering the parallel ohmic pathways in the switch only the silver passivation layer and the copper electrical stabiliser layer on the HTS side of the tape are used. This follows recent work looking at current path sharing in HTS tapes [49]. The resistivities of both layers are taken from Ekin [50]. A graphical representation of the 3D lookup table of calculated resistances at 77.5 K for different magnetic fields is shown in Fig. 7.

The 3D resistivity look-up table is saved into the Matlab workspace and accessed in Simulink by a custom $J_c(T,B)$ block. This block also outputs power in the unit of watts which interfaces well with the Simscape thermal library.

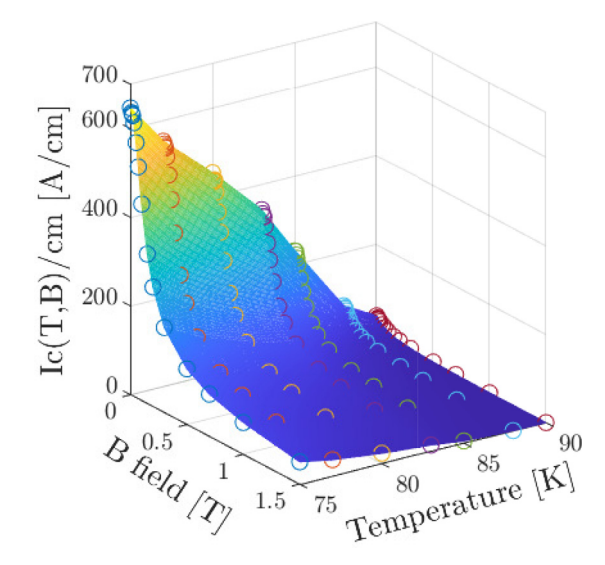


Fig. 6. $I_c(T,B,0)$ /cm data for the SuNAM HCN04200 HTS tape used for the $J_c(B)$ switches in experiment and simulation.

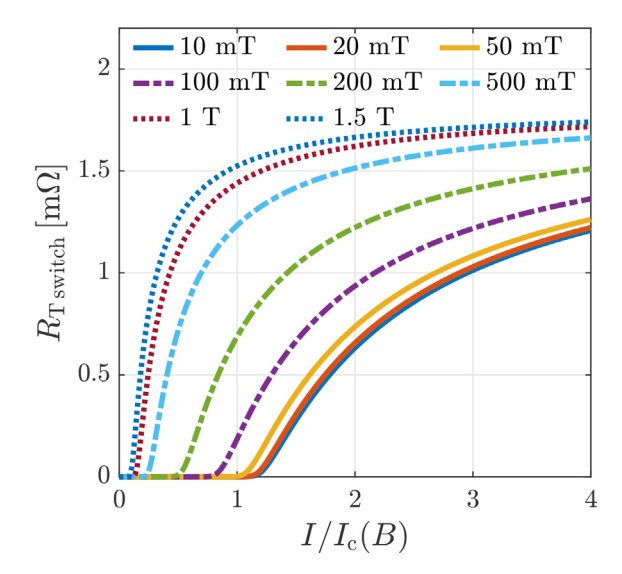


Fig. 7. Resistance of a switch as a function of the applied transport current and perpendicular field at 77 K.

3.4 Thermal considerations

An assumption made for most of the HTS tape is that the temperature does not change significantly due to immersion in LN2. This assumption, as will be shown below, is wildly inaccurate for most TRFPs [43]. In reality, the switching process leads to non-trivial amounts of power when the operational currents are applied, causing significant local heating. In an attempt to include the thermal effects of the experimental system a thermal model has been constructed.

The switch tape is modelled as a heat source whose thermal mass includes all ohmic layers the length and width of the switch tape. The input power used to determine the thermal changes is calculated in the switch block using $P = I^2R$. This heat is then dissipated via the cooling paths available to the switch tape, into the switch magnet core and down the axis of the HTS tape. This is a non-trivial thermal system to model in Simulink as the entire system is submerged in LN2. The thermal bath temperature is assumed to be that of the vapour pressure temperature of LN2 at 1 atmosphere of pressure, 77.343 K [51].

The conduction cooling path via the switch electromagnet is modelled using the combination of both conduction and LN2 convection. To ensure electrical isolation from the switch electromagnet cores during experiment, the cores and switch lengths are wrapped in one layer of Kapton tape each. The simulated heat path from a switch into its associated electromagnet core therefore must include these two layers of Kapton, which are modelled using a Simscape thermal conduction block and the known thermal conductivity and thickness of Kapton tape [50]. The cooling of the switch core itself is via convection cooling in the bath of LN2. The LN2 convection cooling is modelled using a custom Simscape block with a variable heat transfer rate (Q) over an area (A) as;

$$\frac{Q}{A} = c\Delta T^{2.5} \quad [(W/m^2)(K^{-2.5})], \tag{8}$$

where ΔT is the temperature difference between the solid mass (switch core) and the convection medium (liquid nitrogen) and c is a constant with values from 10^2 to 10^3 based on surface condition and orientation [50]. When considering liquid nitrogen convection there are two main regimes, nucleate boiling which ends at roughly $\Delta T=10$ K and film boiling where ΔT increases by more than an order of magnitude in the calculation of Eq. 8. Film boiling is not included in this model as the system does not exceed this threshold when the waveforms in Fig. 2 are used.

To model the tape axis cooling path accurately the cooling capacity of each individual layer in the superconducting tape must be considered in parallel. The individual layers of the tape are modelled as parallel paths over a length of 1 mm using their individual thicknesses and material thermal qualities. These parallel paths are then connected to a portion of tape in the LN2 bath with a thermal mass inclusive of all tape layers. This thermal mass is in contact with the LN2 bath via a layer of Kapton which is included between the tape thermal mass and the liquid nitrogen. Finally, the cooling of the thermal mass of tape is simulated using the nucleate boiling block explained earlier.

The thermal model of the switch outputs the calculated temperature of the switch tape in the units of Kelvin. This temperature is fed back into the Jc(T,B) block allowing for the resistance of the switch tape to be calculated as a function of not only magnetic field but also temperature. All of the thermodynamic values used in the thermal model are taken from Ekin [50] with the exception of silver [52].

4. Experiment and simulation results

Using the input waveforms in Fig. 2 at 1.5 A the experimental system and a simulation were run for 100 s with an initial dead time of 5 s to check for offsets arising from transient and unpredictable DC errors in the experimental measurement system. As previously mentioned the

turns ratio of the experiment (720:12) and simulation are different. The simulation turns ratio of 720:17 was determined by matching the secondary current peaks for the first cycle as shown in Fig. 8(b). This drop in expected current has been touched on recently [53,43]. However, further testing using a dedicated experimental apparatus with multiple variables is required to determine the exact mechanism in a $J_c(B)$ flux pump so that the turns ratio can be modelled analytically. This is expected to be a dynamic effect and will be investigated in detail in later work. Once the turns ratio change is applied, the dynamics of the secondary current matches closely for the first few cycles as shown in Fig. 8(b).

The simulated secondary maintenance phase then departs from the experimental secondary as the transformer is pushed into saturation as seen in Fig. 8(c). The disparity between the experimental and simulated results are due to the imprecise modelling of the transformer where a anhysteretic B(H) curve was used. Future improvements to this model and others like it will require a full hysteretic transformer model likely based on the Jiles-Atherton model [54,55], inclusive of minor hysteretic curves [56] and eddy current losses [57,58]. The authors plan to implement this feature in the future.

The voltages at the switches are shown Fig. 9 where the experimental voltage signals have large inductive spikes corresponding to crosstalk emanating from the up and down current ramps of the switch fields. These spikes visually dominate the complete dataset Fig. 9(a). However, the accuracy of the match between simulation and experiment is made evident when inspecting a limited number of cycles at a time. For instance, the first and last cycles have been plotted in Fig. 9(b) and (c) in the same way as the secondary currents in Fig. 8 (b) and (c).

When ignoring the large spikes, the shapes and amplitudes of the switch voltages match well. In addition, to simply capturing the overall shape, we can now begin to consider the quantitative matching. This is best illustrated by considering the voltage integral per cycle. This integral determines the amount of current that is pumped into the load during the pumping phase and, over a number of cycles, determines the saturation state of the transformer. The series voltages in Fig. 9(c) match in shape but not in integral and as such the transformer is being driven differently to the experiment. This is expected as the transformer model is simplistic as mentioned earlier. The drop off in magnitude of the series switches follows the simulated secondary current in Fig. 8(c), showing that the simulated switches are acting as intended.

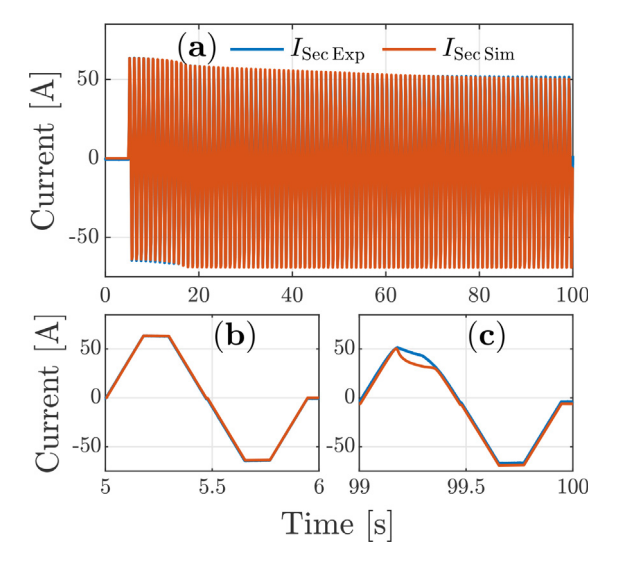


Fig. 8. Experimental and simulated secondary current. Enlarged first and last cycles are shown in (b) and (c) respectively.

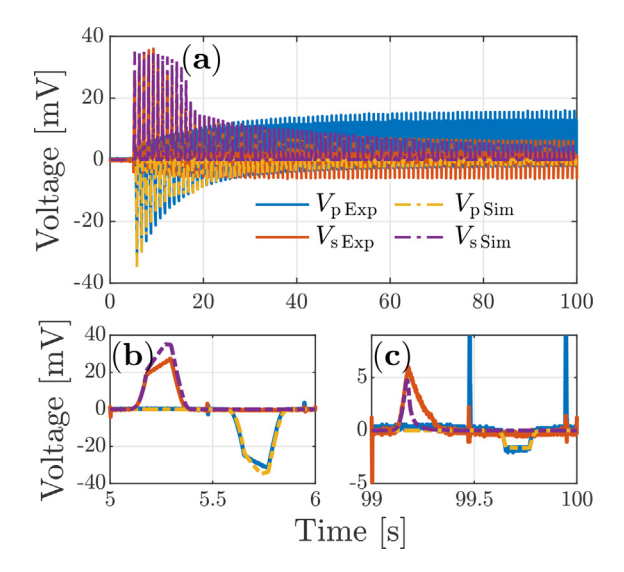


Fig. 9. Experimental and simulated switch voltages. Enlarged first and last cycles are shown in (b) and (c) respectively.

The simulated temperature of the switches shown in Fig. 10(a) can be thought of as a proxy for the total power that the switches create. When comparing the evolving shape of both switches with the voltages in Fig. 9(a) they match in shape over the entire 100 s. The dip then peak in the parallel temperature at about 17 s is an artefact of the simplistic transformer being pushed into a saturated regime faster than happens in the experimental system. This is evident by the lack of this quick change in the experimental parallel voltage in Fig. 9(a). This peak changes the way that the simulated system progresses. For a more direct comparison Fig. 10(b) and (c) show the first and last pump

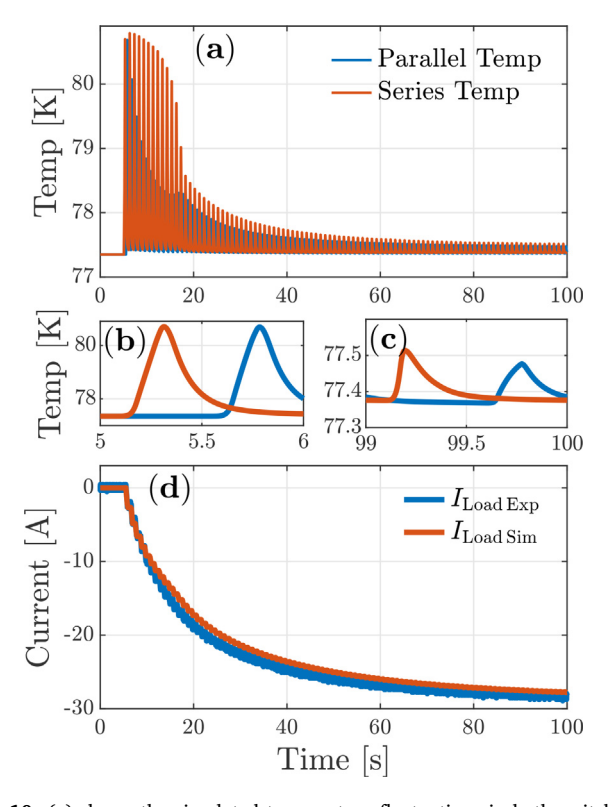


Fig. 10. (a) shows the simulated temperature fluctuations in both switches. (b) and (c) are zoomed in panels showing the first and last pump of the 100 s thermal data. (d) shows the experimental and simulated load current.

cycles of the simulated switch temperature data sets similar to Fig. 8. The effect of the artificial transformer peak is evident in the simulated load current when compared to the experimental case in Fig. 10(d).

Before the dip-peak feature in Fig. 10(a) occurs the pumping matches well. during the dip the load is pumped less hard per cycle until it reaches the peak at which point it is pumped hard for a few cycles. The load current curve then settles after a few cycles to match the experimental curve albeit now offset by ~ 1 to 2 A. Excluding the effects of the transformer the model predicts the way that the experimental system evolves quite accurately.

To illustrate the importance of the thermal component in a $J_c(B)$ switched TRFP the experimental and simulated lines in Fig. 10(d) have been plotted along side a simulated load current where the temperature was fixed to the bath temperature in Fig. 11.

Usually when attempting to model a HTS flux pump, especially one with $J_c(B)$ switches many will fail to get to generate the experimentally observed high resistance. Usually stating that the tape has degraded as a way of artificially decreasing their switch I_c . This subsequently increases the switch resistance and thus load current. The comparison in Fig. 11 shows that this method of matching load current via artificial tape degradation is unnecessary and potentially covering up an important aspect of $J_c(B)$ rectification: the interaction of the thermal processes inside the HTS tape. The authors therefore urge readers intending to model a HTS flux pump of any kind to always consider the thermal effects of the system even if it is not the initial driving factor, as a change of only a few degrees can have a profound effect on the evolution of a flux pumps performance.

To inspect the robustness of the simulation three different primary currents of 1.5, 1.3 and 1.1 A were used. The comparison between the simulated and experimental results of these different primary inputs are shown in Fig. 12.

The 1.1 A experimental and simulated data match almost identically this is due to the transformer never being pushed far into the highly non-linear portion of the anhysteretic B(H) curve used. The 1.3 A data has a large discrepancy centred around 30 s. This is the transformer problem manifested strongly due to the system being in a 'sweet spot' in relation to the B(H) curve of the transformer. This further illustrates the need for a more realistic transformer model. The mismatch in the 1.5 A data is much smaller around 17 s having been pushed through this region relatively quickly when compared to the 1.3 A data sets.

Despite the discrepancy originating from the simulated anhysteretic transformer, the model has been shown to be capable of delivering qualitatively accurate predictions of the output current from a

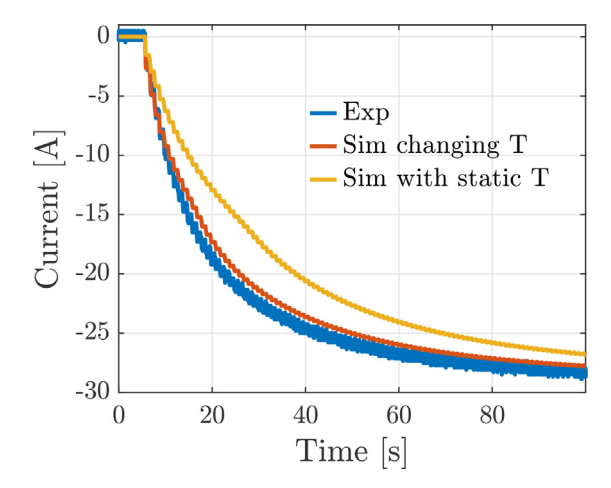


Fig. 11. Experimental load current compared to simulations with a dynamic thermal model and a static thermal model at the LN2 bath temperature.

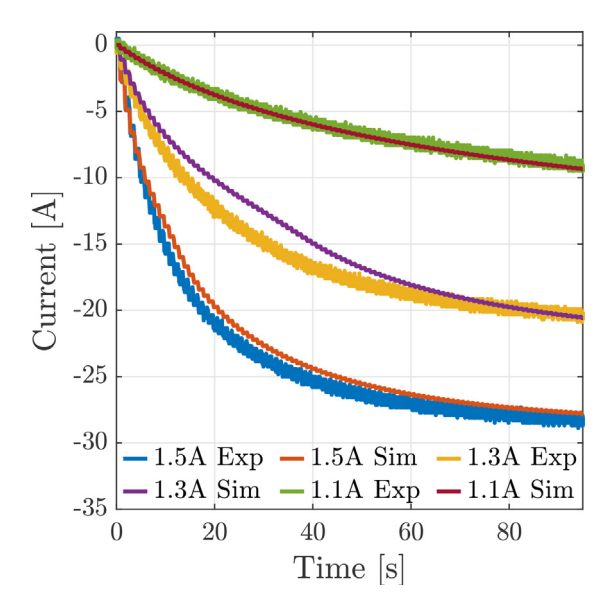


Fig. 12. Experimental and simulated load currents using three different primary currents of 1.5, 1.3 and 1.1 A.

 $J_c(B)$ switched half wave TRFP. With a robust and complete transformer model this simulation will become quantitatively predictive allowing it to be used to plan future TRFP designs. The authors believe this modelling technique provides a framework for the next generation of TRFPs by allowing different configurations, superconducting elements, and waveforms to be rapidly benchmarked through the use of our custom Simscape blocks.

A potential additional source of error in the presented model is the exclusion of AC loss and frequency dependent I_c effects within the HTS circuit [59]. As an initial estimate these effects were not included due to the frequency of operation being 1 Hz. However, the addition of AC effects within the presented model is planned for future work by the authors.

The total compute time for a 100 s simulation was less than a minute as measured by the "tic toc" Matlab functions (20 to 40 s depending on if the session is a fresh Matlab/Simulink boot) with a data resolution of 1 ms, using an i5-1135G7 cpu at 2.4 GHz and a single thread. The total memory used for the 100 s simulation outputting

all presented data and some others omitted was ~ 0.1 MB. The current code has some switchable methods to reduce the compute time and memory usage which were not used, and for the sake of brevity have been omitted. These methods only become applicable when batching (conducting variable sweeps or conducting a Monte Carlo like simulation) or when simulating a flux pumps performance over a much longer time scale (hours to days) than what is presented in this work.

5. Conclusion

Throughout this work a model capable of simulating a $J_c(B)$ switched half-wave transformer rectifier flux pump has been introduced. This work is set apart from previous works by the use of experimentally derived lookup tables in conjunction with custom magnetic and electric Simscape blocks combined with thermal considerations. While the model could be further improved through the implementation of a more realistic transformer model it can act as a robust framework for future simulations of HTS TRFPs of various types. The authors foresee the simulation presented here as being extremely useful for understanding the physical processes of HTS TRFPs, directing iterative optimisation of existing systems and the successful planning of future systems.

Declaration of Competing Interest

The authors declare that they have no known competing financial interests or personal relationships that could have appeared to influence the work reported in this paper.

Acknowledgment

This work was supported by the New Zealand Ministry of Business, Innovation and Employment (MBIE) under Contract No. RTVU1707 and Strategic Science Investment Fund 'Advanced Energy Technology Platforms' Contract RTVU2004.

Appendix A. Simulink visual code images

The following images are screen grabs of the Simulink code discussed in this work.

See Figs. A.13, A.14, A.15 and A.16.

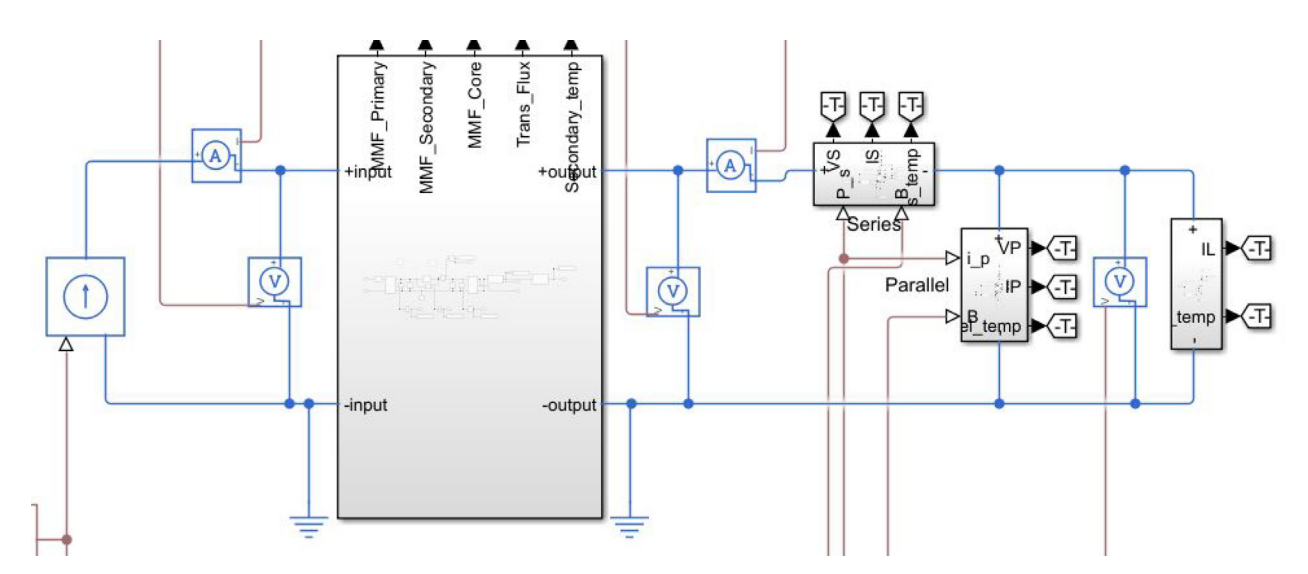


Fig. A.13. Total simulink model consisting of electrical circuit connected to the transformer (large box in the middle), the series and parallel switches and the load.

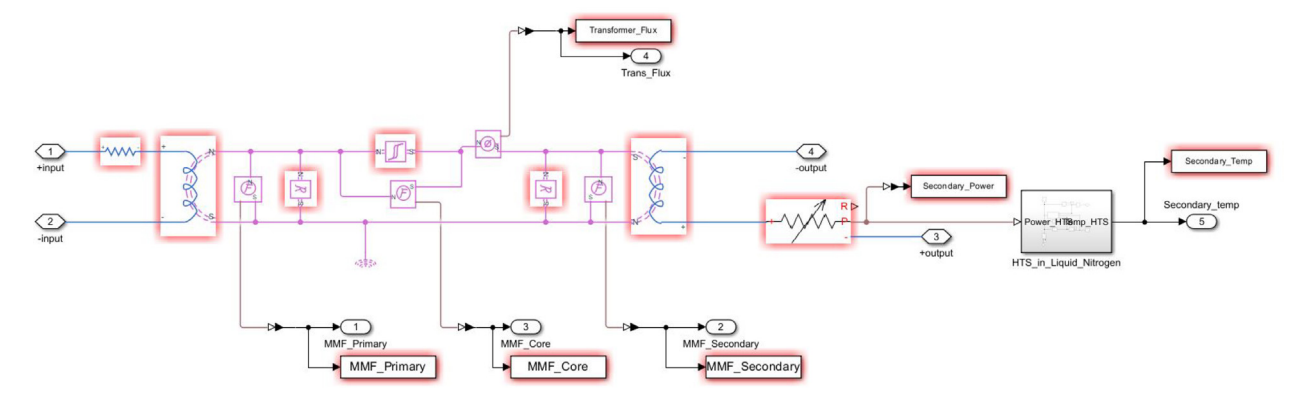


Fig. A.14. Simulink model of the transformer inclusive of the superconducting block on the secondary.

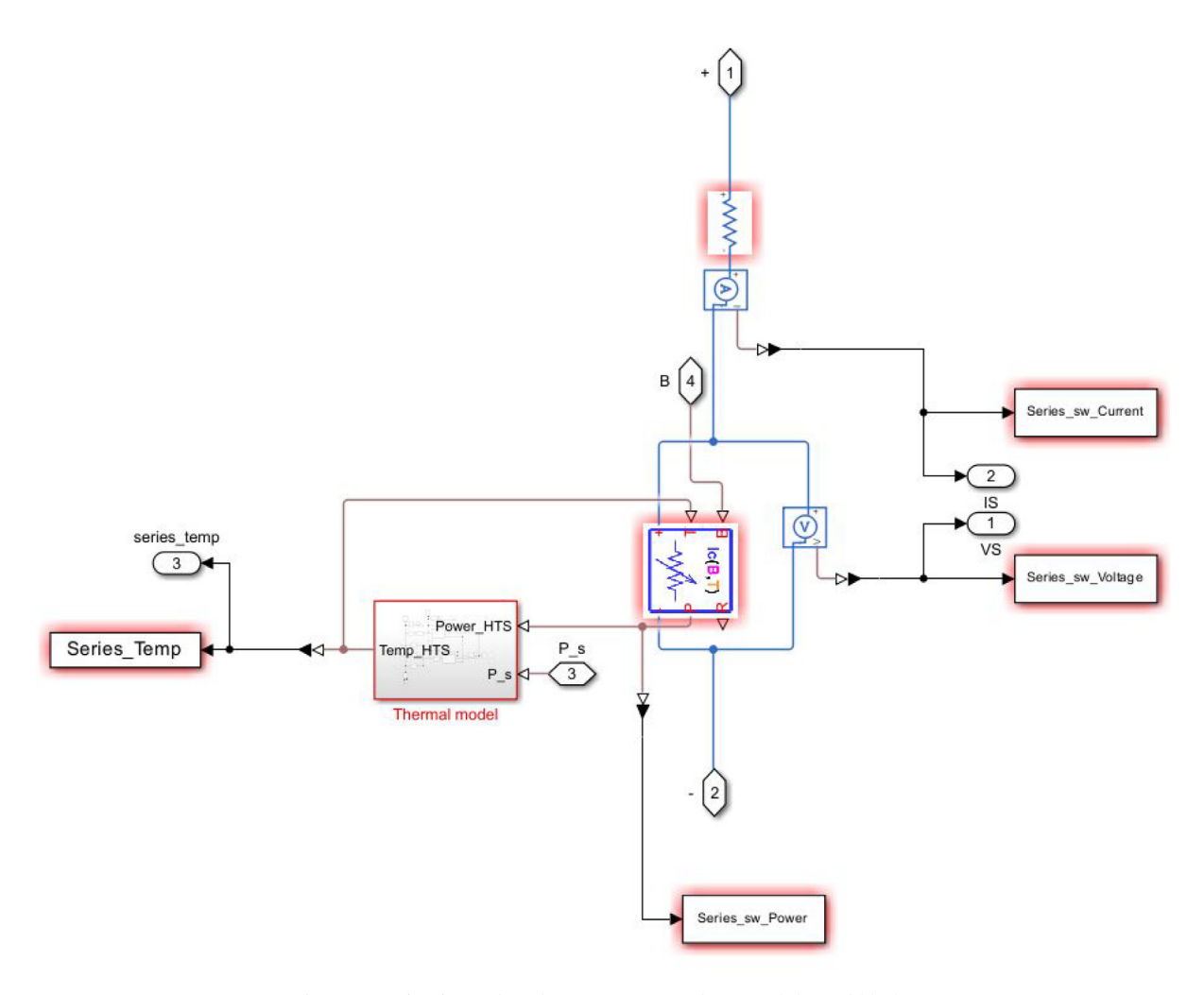


Fig. A.15. $J_c(B,T)$ switch with custom superconductor and thermal blocks.

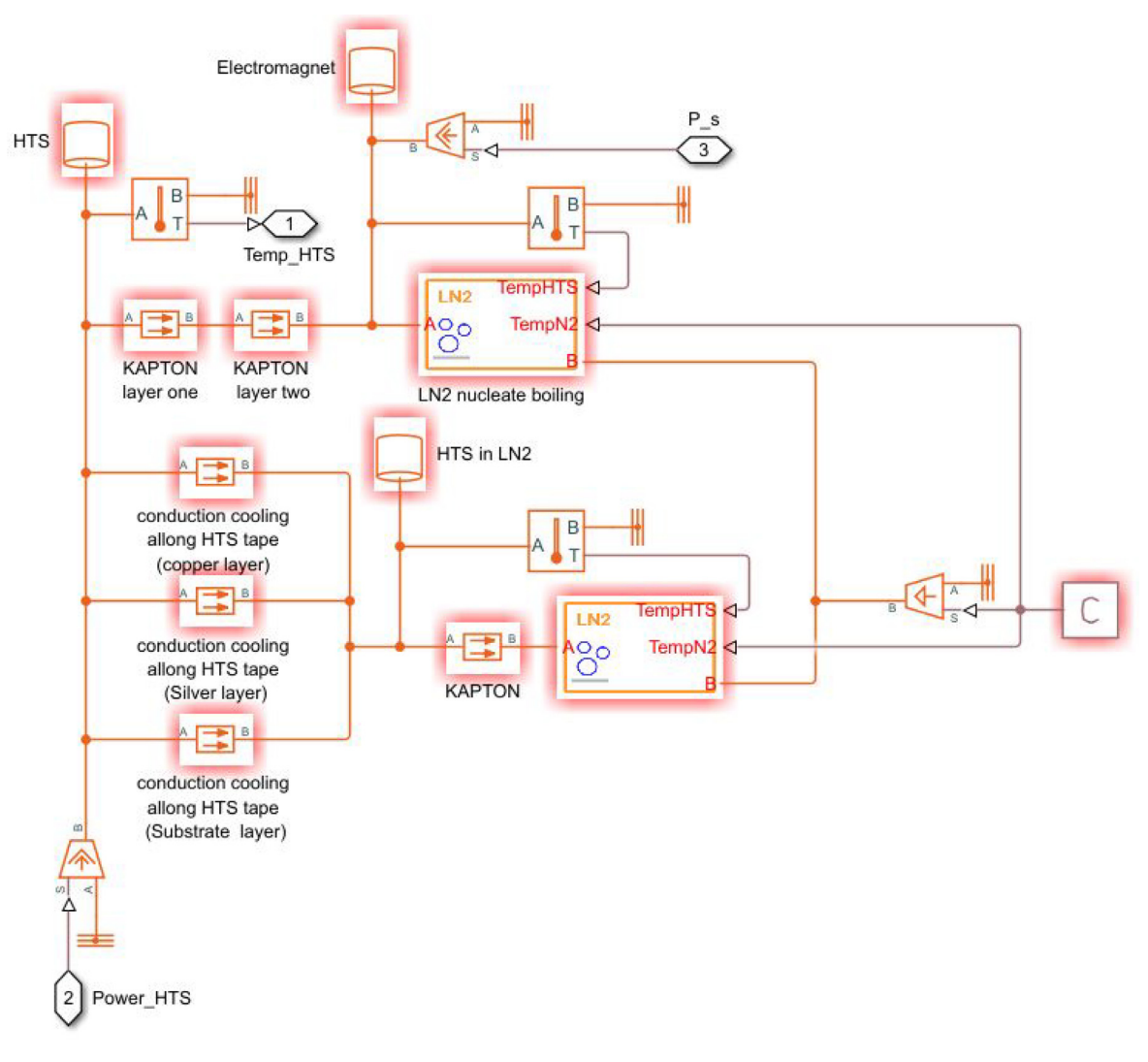


Fig. A.16. Thermal model of the $J_c(B,T)$ switch submerged in liquid nitrogen and in contact with the electromagnet core.

References

- [1] Bruzzone P, Fietz WH, Minervini JV, Novikov M, Yanagi N, Zhai Y, et al. High temperature superconductors for fusion magnets. Nucl Fusion 2018;58 (10):103001. https://doi.org/10.1088/1741-4326/aad835.
- [2] Maeda H, Yanagisawa Y. Recent developments in high-temperature superconducting magnet technology (review). IEEE Trans Appl Supercond 2014;24(3):1–12. https://doi.org/10.1109/TASC.2013.2287707.
- [3] Parkinson B. Design considerations and experimental results for mri systems using hts magnets. Supercond Sci Technol 2016;30(1):014009. https://doi.org/10.1088/0953-2048/30/1/014009.
- [4] Wikus P, Frantz W, Kümmerle R, Vonlanthen P. Commercial gigahertz-class nmr magnets. Supercond Sci Technol 2022;35(3):033001. https://doi.org/10.1088/1361-6668/ac4951.
- [5] Devred A, Baynham DE, Bottura L, Chorowski M, Fabbricatore P, Leroy D, et al. High field accelerator magnet r&d in europe. IEEE Trans Appl Supercond 2004;14 (2):339–44. https://doi.org/10.1109/TASC.2004.829121.
- [6] Schwartz J, Effio T, Liu X, Le QV, Mbaruku AL, Schneider-Muntau HJ, et al. High field superconducting solenoids via high temperature superconductors. IEEE Trans Appl Supercond 2008;18(2):70–81. https://doi.org/10.1109/TASC.2008.921363.
- [7] Iwasa Y. Case studies in superconducting magnets: design and operations issues.
 2nd ed. New York, NY: Springer; 2009. https://doi.org/10.1007/b112047.
- [8] Weijers HW, Trociewitz UP, Markiewicz WD, Jiang J, Myers D, Hellstrom EE, et al. High field magnets with hts conductors. IEEE Trans Appl Supercond 2010;20 (3):576–82. https://doi.org/10.1109/TASC.2010.2043080.
- [9] McFee R. Optimum input leads for cryogenic apparatus. Rev Sci Instrum 1959;30 (2):98–102. https://doi.org/10.1063/1.1716499.
- [10] Rice JHP, Geng J, Bumby CW, Weijers HW, Wray S, Zhang H, et al. Design of a 60 ka flux pump for fusion toroidal field coils. IEEE Trans Appl Supercond 2022;32 (4):1–5. https://doi.org/10.1109/TASC.2021.3137762.

- [11] Wen Z, Zhang H, Mueller M. High temperature superconducting flux pumps for contactless energization. Crystals 2022;12(6):766.
- [12] Ohki K, Nagaishi T, Kato T, Yokoe D, Hirayama T, Ikuhara Y, et al. Fabrication, microstructure and persistent current measurement of an intermediate grown superconducting (igs) joint between rebco-coated conductors. Supercond Sci Technol 2017;30(11):115017. https://doi.org/10.1088/1361-6668/aa8e65.
- [13] Bagrets N, Augieri A, Celentano G, Tomassetti G, Weiss K, Corte AD. Investigation of rebco conductor tape joints for superconducting applications. IEEE Trans Appl Supercond 2015;25(3):1–5. https://doi.org/10.1109/TASC.2014.2373055.
- [14] Bagrets N, Nast R, Fournier-Lupien JH, Sirois F, Celentano G, Weiss KP. Current transfer length and interfacial resistance between superconductors and metals in commercial rebco tapes and cables. IEEE Trans Appl Supercond 2021;31(6):1–8. https://doi.org/10.1109/TASC.2021.3085359.
- [15] Skarba M, Pekarcíková M, Frolek L, Cuninková E, Necpal M. Thermal cycling of (re)bco-based superconducting tapes joined by lead-free solders. Materials 2021:14(4):1052.
- [16] Coombs TA, Geng J, Fu L, Matsuda K. An overview of flux pumps for hts coils. IEEE Trans Appl Supercond 2017;27(4):1–6. https://doi.org/10.1109/TASC.2016.2645130.
- [17] van de Klundert LJM, ten Kate HHJ. Fully superconducting rectifiers and fluxpumps part 1: Realized methods for pumping flux. Cryogenics 1981;21 (4):195–206. https://doi.org/10.1016/0011-2275(81)90195-8.
- [18] van de Klundert LJM, ten Kate HHJ. On fully superconducting rectifiers and fluxpumps. a review. part 2: Commutation modes, characteristics and switches. Cryogenics 1981;21(5):267–77. https://doi.org/10.1016/0011-2275(81)90002-3.
- [19] Hoffmann C, Pooke D, Caplin AD. Flux pump for hts magnets. IEEE Trans Appl Supercond 2011;21(3):1628–31. https://doi.org/10.1109/TASC.2010.2093115.
- [20] The National High Magnetic Field Laboratory Applied Superconductivity Center: Plots. [online] Available at: https://nationalmaglab.org/magnet-development/applied-superconductivity-center/plots [Accessed: 5/2022].

- [21] Jiang Z, Hamilton K, Amemiya N, Badcock RA, Bumby CW. Dynamic resistance of a high-tc superconducting flux pump. Appl Phys Lett 2014;105(11):112601. https://doi.org/10.1063/1.4895732.
- [22] Bumby CW, Pantoja AE, Sung HJ, Jiang Z, Kulkarni R, Badcock RA. Through-wall excitation of a magnet coil by an external-rotor hts flux pump. IEEE Trans Appl Supercond 2016;26(4):1–5. https://doi.org/10.1109/TASC.2016.2526605.
- [23] Hamilton K, Pantoja AE, Storey JG, Jiang Z, Badcock RA, Bumby CW. Design and performance of a squirrel-cage dynamo-type hts flux pump. IEEE Trans Appl Supercond 2018;28(4):1–5. https://doi.org/10.1109/TASC.2018.2805161.
- [24] Bai Z, Yan G, Wu C, Ding S, Chen C. A novel high temperature superconducting magnetic flux pump for mri magnets. Cryogenics 2010;50(10):688–92. https://doi.org/10.1016/j.cryogenics.2010.06.021.
- [25] Oomen MP, Leghissa M, Ries G, Proelss N, Neumueller HW, Steinmeyer F, et al. Hts flux pump for cryogen-free hts magnets. IEEE Trans Appl Supercond 2005;15 (2):1465–8, https://doi.org/10.1109/TASC.2005.849129.
- [26] Park D, Lee J, Bascuñán J, Michael PC, Iwasa Y. Hts shim coils energized by a flux pump for the mit 1.3-ghz lts/hts nmr magnet: Design, construction, and results of a proof-of-concept prototype. IEEE Trans Appl Supercond 2018;28(3):1–5. https:// doi.org/10.1109/TASC.2018.2799182.
- [27] Geng J, Bumby CW, Badcock RA. Maximising the current output from a self-switching ka-class rectifier flux pump. Supercond Sci Technol 2020;33(4):045005. https://doi.org/10.1088/1361-6668/ab6957.
- [28] Mataira RC, Ainslie MD, Badcock RA, Bumby CW. Origin of the dc output voltage from a high-tc superconducting dynamo. Appl Phys Lett 2019;114(16):162601. https://doi.org/10.1063/1.5085226.
- [29] Homer G, Houzego P, Scott C, Wilson M. A thermally switched flux pump. IEEE Trans Magn 1975;11(2):576–9. https://doi.org/10.1109/TMAG.1975.1058693.
- [30] Geng J, Coombs TA. An hts flux pump operated by directly driving a superconductor into flux flow region in the e-j curve. Supercond Sci Technol 2016;29(9):095004. https://doi.org/10.1088/0953-2048/29/9/095004.
- [31] Geng J, Coombs TA. Mechanism of a high-tc superconducting flux pump: Using alternating magnetic field to trigger flux flow. Appl Phys Lett 2015;107 (14):142601. https://doi.org/10.1063/1.4932950.
- [32] Ma J, Geng J, Coombs TA. Flux pumping for non-insulated and metal-insulated hts coils. Supercond Sci Technol 2018;31(1):015018. https://doi.org/10.1088/1361-6668/aa99f2
- [33] Geng J, Badcock RA, Bumby CW. A wireless rectifier for inductively energizing high direct-current high-temperature superconducting magnets. IEEE Trans Industr Electron 2021;68(4):3273–81. https://doi.org/10.1109/TIE.2020.2982095.
- [34] Leuw B, Geng J, Rice JHP, Moseley DA, Badcock RA. A half-wave superconducting transformer-rectifier flux pump using j_c(b) switches. Supercond Sci Technol 2022;35(3):035009. https://doi.org/10.1088/1361-6668/ac4f3d.
- [35] The MathWorks Inc., Simulink. [online] Available at: https://mathworks.com/products/simulink.html [Accessed: 3/2022].
- [36] Gawith JDD, Geng J, Li C, Shen B, Zhang X, Ma J, et al. A half-bridge hts transformer–rectifier flux pump with two ac field-controlled switches. Supercond Sci Technol 2018;31(8):085002. https://doi.org/10.1088/1361-6668/aac86d.
- [37] Gawith J, Geng J, Ma J, Shen B, Li C, Coombs TA. Hts transformer–rectifier flux pump optimization. IEEE Trans Appl Supercond 2019;29(5):1–5. https://doi.org/10.1109/TASC.2019.2904444.
- [38] Li C, Wang S, Jia H, He J, Li B, Coombs TA. Impacts of the saturated transformer on the hts flux pump. IEEE Trans Appl Supercond 2021;31(8):1–4. https://doi.org/10.1109/TASC.2021.3090350.
- [39] Patel I, Shah A, Öztürk Y, Shen B, Hao L, Yang J, et al. Matlab implementation of an hts transformer-rectifier flux pump using hts dynamic voltage switches. IEEE Trans Appl Supercond 2022;32(4):1–4. https://doi.org/10.1109/TASC.2021.3131135.
- [40] Zhai Y, Ma G, Deng Y, Sun C, Li Y, Zhou P. Modeling and characteristics investigation of self-regulating hts flux pump. Cryogenics 2022;124:103486. https://doi.org/10.1016/j.cryogenics.2022.103486.

- [41] Nowicki M. Anhysteretic magnetization measurement methods for soft magnetic materials. Materials (Basel) 2018;11(10). https://doi.org/10.3390/ma11102021.
- [42] Jiles DC, Atherton DL. Theory of ferromagnetic hysteresis. J Magn Magn Mater 1986;61(1):48–60. https://doi.org/10.1016/0304-8853(86)90066-1.
- [43] Clarke J, Leuw B, Venuturumilli S, Mallett B, Moseley DA, Bumby C, et al. Temperature dependent performance of a conduction-cooled jc(b) transformer-rectifier flux pump. IEEE Trans Appl Supercond 2023;33(5):1–6. https://doi.org/10.1109/TASC.2023.3247376.
- [44] MacManus-Driscoll JL, Wimbush SC. Processing and application of high-temperature superconducting coated conductors. Nat Rev Mater 2021;6 (7):587–604. https://doi.org/10.1038/s41578-021-00290-3.
- [45] Galván DH, Avalos-Borja M, Farías MH, Cota-Araiza L, Reyes A, Cruz-Reyes J, et al. Effect of silver in y1ba2cu3o7-x samples. J Mater Sci 1994;29(10):2713–8. https://doi.org/10.1007/BF00356822.
- [46] Rupich MW, Li X, Sathyamurthy S, Thieme CLH, DeMoranville K, Gannon J, et al. Second generation wire development at amsc. IEEE Trans Appl Supercond 2013;23 (3). https://doi.org/10.1109/TASC.2012.2235495. 6601205-6601205.
- [47] Lacroix C, Sirois F, Slimani K, Cave J. Electro-thermal response of 2g hts coated conductors subjected to current pulses. IEEE Trans Appl Supercond 2013;23:6601605. https://doi.org/10.1109/TASC.2013.2238285. 5 pp..
- [48] Strickland NM, Wimbush SC, Pantoja A, Pooke DM, Fee M, Chamritskii V, et al. Extended-performance supercurrent cryogen-free transport critical-current measurement system. IEEE Trans Appl Supercond 2021;31(5):1–5. https://doi.org/10.1109/TASC.2021.3060355.
- [49] Zhang H, Suo H, Wang L, Ma L, Liu J, Zhang Z, et al. Database of the effect of stabilizer on the resistivity and thermal conductivity of 20 different commercial rebco tapes. Supercond Sci Technol 2022;35(4):045016. https://doi.org/10.1088/ 1361-6668/ac5784.
- [50] Ekin J. Experimental techniques for low-temperature measurements: cryostat design, material properties and superconductor critical-current testing, OUP Oxford; 2006. URL https://books.google.co.nz/books?id = Q9tmZQTDPiYC.
- [51] Moussa MR, Muijlwijk R, Van Dijk H. The vapour pressure of liquid nitrogen. Physica 1966;32(5):900–12. https://doi.org/10.1016/0031-8914(66)90021-8.
- [52] Smith DR, Fickett FR. Low-temperature properties of silver. J Res Natl Inst Stand Technol 1995;100(2):119–71. https://doi.org/10.6028/jres.100.012.
- [53] Zhai Y, Zhou P, Li J, Sun C, Li Y, Xiao L, et al. Performance investigation of contactless self-regulating hts flux pump. IEEE Trans Appl Supercond 2021;31 (5):1–5. https://doi.org/10.1109/TASC.2021.3073531.
- [54] Li W, Kim IH, Jang SM, Koh CS. Hysteresis modeling for electrical steel sheets using improved vector jiles-atherton hysteresis model. IEEE Trans Magn 2011;47 (10):3821–4. https://doi.org/10.1109/TMAG.2011.2158296.
- [55] Lihua Z, Jingjing L, Qingxin Y, Jianguo Z, Koh CS. An improved magnetostriction model for electrical steel sheet based on jiles—atherton model. IEEE Trans Magn 2020;56(3):1–4. https://doi.org/10.1109/TMAG.2019.2951824.
- [56] Mazgaj W, Sierzega M, Szular Z. Approximation of hysteresis changes in electrical steel sheets. Energies 2021. https://doi.org/10.3390/en14144110. URL https://mdpi-res.com/d_attachment/energies/energies-14-04110/article_deploy/energies-14-04110-v3.pdf?version=1626240682.
- [57] Gao Y, Shibauchi T, Gotoh Y, Guan W, Muramatsu K. Dynamic hysteresis calculation of silicon steel considering dc hysteresis and anomalous eddy current loss. In: 2022 IEEE 20th Biennial Conference on Electromagnetic Field Computation (CEFC); 2022. p. 1–2. https://doi.org/10.1109/CEFC55061.2022.2940876. https://ieeexplore.ieee.org/stampPDF/getPDF.jsp?tp = & arnumber = 9940876&ref = .
- [58] Fujiwara T, Tahara R. Eddy current modeling of silicon steel for use on spice. IEEE Trans Magn 1995;31(6):4059–61. https://doi.org/10.1109/20.489861.
- [59] Thakur KP, Raj A, Brandt EH, Kvitkovic J, Pamidi SV. Frequency-dependent critical current and transport ac loss of superconductor strip and roebel cable. Supercond Sci Technol 2011;24(6):065024. https://doi.org/10.1088/0953-2048/24/6/065024.